Pressure wrist pulse signal analysis by sparse decomposition using improved Gabor function

Zhixing Jiang [a,c], Chaoxun Guo [a,b], David Zhang [a,b,*]

[a] *The Chinese University of Hong Kong Shenzhen, Shenzhen, China*
[b] *Shenzhen Research Institute of Big Data, Shenzhen, China*
[c] *University of Science and Technology of China, Hefei, China*

ARTICLE INFO

ABSTRACT

Background and objective: In traditional Chinese medicine and Ayurvedic medicine, wrist pulse wave fluctuations are an important indicator for distinguishing different health states. Owing to the development of modern sensing technology, computational methods have been used in the analysis of pulse wave signals. The description and quantification of the peaks in the pulse wave is significant for the identification of health status.

Methods: In this study, we decomposed the pressure pulse waveform of the radial artery into several components by sparse decomposition with an improved Gabor function. To better represent the position, shape, and relationship of the peaks, we designed an improved Gabor function structure based on the characteristics of the pulse waveform to generate a time-frequency dictionary. Compared with conventional representation methods, the shape of the Gabor function is more variable. In addition, owing to the limitation of windowing, the Gabor function can reduce the influence on other positions when it represents a specific position. Feature vectors consisting of decomposed components can be used for computerized pulse signal analysis and disease diagnosis.

Results: In the binary classification of healthy and diseased pulse signals, the proposed method achieved the best results for health/diabetes, health/cardiac disease, health/hypertension, and health/nephropathy with accuracies of 93.54%, 73.42%, 88.42%, and 82.28%, respectively. The multi-classification performance of the different types of features was evaluated by six classifiers, and the proposed method obtained the highest classification performance with support vector machine-radial basis function for both balanced and imbalanced data.

Conclusions: The results indicated that the proposed method enabled to obtain a smaller representation error and exhibited superior performance in distinguishing between the signals collected from patients and healthy individuals. Moreover, for the multi-classification of the pulse signals, the proposed method performed better than the state-of-the-art methods.

1. Introduction

The wrist pulse is an important physiological signal that contains significant information about health status. In traditional Chinese pulse diagnosis, physicians place their index finger, middle finger, and third finger on different positions of the radial artery, called Cun, Guan, and Chi, respectively, to sense the pulse [1,2]. Based on the rhythm and force of the pulse and their personal experience, they evaluate the health situation or disease types of the patients, which requires years of accumulation of knowledge and practice. As the diagnosis results highly rely on the subjectivity of physicians, the pulse diagnosis is a skill that takes a long time to master and may lead to significant variations in diagnosis results for different physicians, which is not in line with the development of modern medicine. An objective evaluation of the wrist pulse should consist of acquiring the signals by sensors and analyze the information contained in the digital signals using computerized methods [3].

Traditional Chinese medicine (TCM) physicians classify the wrist pulse sensed by the fingers into more than 20 categories, which differ in rhythm, force, shape, etc. To objectively identify the relationship between the different pulse signals and corresponding

* Corresponding author at: The Chinese University of Hong Kong Shenzhen, Shenzhen, China.
E-mail address: davidzhang@cuhk.edu.cn (D. Zhang).

health conditions, some studies have been conducted to extract several features that can be used to recognize the conditions by classifiers. Because the fluctuation information of pulse waves contains rich physiological and pathological information, some methods have been proposed to measure the fluctuation information of a single-cycle pulse signal.

To describe the fluctuation information such as main peak, tidal wave, and dicrotic wave in a single-cycle pulse signal, Xu detected several key points and computed some statistical values based on the relationship of those points to recognize the different pulse waveform types [4]. This type of method is widely used in wrist pulse analysis because the time-domain statistics of the wrist pulse can directly reflect the physiological characteristics of signals. However, owing to the fuzziness or disappearance of some key points and the influence of noise, the accuracy of key point detection is reduced, resulting in an error in feature extraction, which affects the reliability of subsequent analyses.

The methods of model fitting are further proposed to solve the problem of inaccurate key point detection. Because the single-cycle pulse wave signal is a smooth curve in shape, these methods usually use multiple curves with different shapes to fit the signal. After fitting the signal and establishing a mathematical model, the model parameters are extracted as features to measure the physiological and pathological information contained in the signal. Chen adopted a two-term Gaussian mixture model (GMM) to fit the peaks in the pulse signal, and the modeling parameters were then taken as features [5]. They also proposed a feature selection scheme to eliminate closely correlated features. Evidently, different studies use GMMs with different numbers of terms to model the signal owing to the difference in the number of peaks in the signals. Liu discussed the optimum combination of Gaussian functions that compose the arterial pressure waveform and found that it is credible to use three positive Gaussian functions to decompose and model the signal [6]. Shin found that the specific parameter of the Gaussian model is the most significant feature for distinguishing patients with chronic gastritis pulse signals and healthy pulse signals [7].

Trigonometric functions are also used to represent pulse wave signals. In contrast to using a Gaussian function to fit a single peak, Jiang proposed a discrete Fourier series model (DFSM), which uses trigonometric function curves with different frequencies and amplitudes to represent the overall signal [8]. Compared with GMM, the model can obtain a reduced representation error, and the ability of model parameters to distinguish diseases is better than that of similar methods. Nevertheless, in both GMM and DFSM, a single curve type cannot better represent the signal adaptively owing to the inherent structural constraints and low morphological adjustability. Different fitting curves introduce representation errors to each other, reducing the ability of the models to represent the original signal.

In addition to using single-cycle signals for feature extraction, some researchers have also analyzed a set of single-cycle signals and continuous signals. Wang used principal component analysis (PCA) to extract the main projection direction of the pulse waveform set and used eigenvectors as features [9]. To explore the relationship between continuous Doppler ultrasound blood flow signal of the wrist radial artery and pathological information of different organs, Zhang adopted the Hilbert-Huang transform for the pulse signal to extract time-frequency features [10]. Because the wrist pulse signal is regarded as a signal composed of components of different frequencies, wavelet analysis is used for multi-resolution analysis of continuous pulse wave signals [11].

In summary, owing to the diversity and noise of the pulse waveform, the accuracy of the key point detection is difficult to guarantee, resulting in inaccurate characteristic points for feature extraction. The modeling methods directly represent the main components of the pulse waveform, such as the main peak, tidal wave, dicrotic wave, outline, and detail, to avoid errors in key point detection. However, the representation component can only roughly represent meaningful information in the pulse waveforms owing to the inherent limitations. Therefore, a technique that can enhance the description of the peaks in the pulse waveform is required.

In this study, we propose a novel representation method based on sparse decomposition with time-frequency atoms for a wrist pulse waveform. The proposed method, which combines the advantages of GMM and DFSM, decomposes the pulse waveform signal into several independent components with certain physiological significance. Compared with previous modeling methods presented in [5,6,7], the fitting curves are symmetrical structures generated by the Gaussian function, where the atoms generated by the Gabor function have an asymmetric structure and the morphology is more adjustable, which can avoid the introduction of additional components at other positions when representing the local structure. In contrast to the methods introduced in [8], whose representation components include both low and high frequencies, the low-frequency atoms used in the proposed method can better represent the main peak, tidal wave, dicrotic wave, etc. in the pulse signal. Therefore, our method enables to obtain a smaller representation error and describes physiological information more clearly and accurately.

The remainder of this paper is organized as follows. Section 2 introduces the wrist pulse signal used in this study. Section 3 describes previous related works, including the GMM and DFSM. In Section 4, the motivation and method of pulse waveform sparse decomposition are presented. Section 5 reports several results to evaluate the proposed pulse signal analysis method, followed by the conclusion in Section 6.

2. Wrist pulse signal acquisition and processing

### 2.1. Wrist pulse signal acquisition

In this study, we used a modified multi-channel pulse acquisition platform proposed in [12] to synchronously collect the pulse signals at Cun, Guan, and Chi. Compared with the photoelectricity sensor and Doppler ultrasonic sensor, the working principle of the pressure sensors used in [12] is similar to that of TCM in perceiving the pulse.

Each sample was collected using the same process to avoid differences caused by non-physiological factors. The position of Guan, which is at the distal end of the radius, was first found by the testers finger. Subsequently, the positions of Cun and Chi were automatically fixed by the acquisition platform. Then, the contact pressure was adjusted for each channel to collect the wrist pulse signal at an appropriate amplitude. In general, the acquisition time was no less than 30 s to ensure that sufficient effective cycles were collected. To collect as much valid information as possible, we set the sampling frequency to 500 Hz, which can theoretically collect the components below 250 Hz.

Although multi-channel signals contain more information than a single channel, it is difficult to collect high-quality pulse signals at three positions simultaneously in actual applications. Because the problem of missing data is not within the scope of this study, we took Guan's signals as an example to introduce the wrist pulse analysis methods, which are also applicable to the signals of Cun and Chi.

2.2. Wrist pulse signal preprocessing

The original pulse signal is very weak and can be easily corrupted by noise. Electrical circuits, such as the filter and amplifier
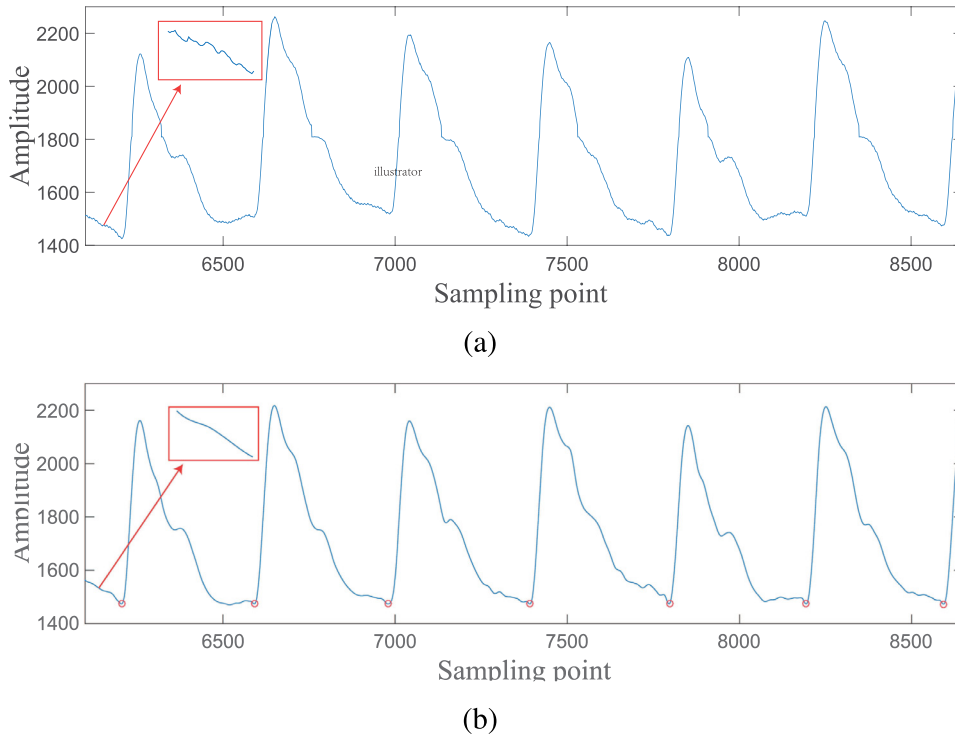
Fig. 1. Partially enlarged view of the continuous multi-cycle pressure wrist pulse signal: (a) original pulse signal with different noise, (b) pulse signal with both high- and low-frequency noises removed.

circuit, introduce high-frequency power frequency noise to the signal. Because the pressure sensors are in direct contact with the skin, the noises generated by respiratory waves, speech, coughing, and muscle jitter were also recorded. These noises with different frequencies need to be removed before feature extraction to avoid waveform distortion and key point detection errors.

In this study, we used wavelet decomposition and cubic spline interpolation to remove high- and low-frequency noises, respectively [13]. Fig. 1(a) shows a typical pressure wrist pulse signal. To remove the power frequency noise, the original signal was denoised by a four-level *sym*8 wavelet transform, whose decomposition coefficients were quantified using a soft threshold based on Shannon entropy for each level. Then, an improved iterative sliding window algorithm was adopted to detect the pacemakers as the segmentation points that were used by cubic spline interpolation to fit the baseline drift caused by the respiratory wave [14]. Pacemaker refers to the starting point of left ventricular ejection into the aorta. In most studies of pulse wave signal analysis, it is selected as the segmentation point of a single-cycle pulse wave signal. After eliminating the drift component in the signal [8], all the segmentation points marked by the red cycles in Fig. 1(b) were maintained in the same horizontal line to improve the similarity between cycles and the quality of the average cycle.

As a periodic physiological signal, there are certain differences in the amplitude and length of each cycle. To reduce the complexity of the subsequent analysis, a unified normalization operation was performed for each discrete cycle. As shown in Fig. 2(a), we normalized the amplitude to [0,1] and the length to $N = [1, 64]$ for the cycles, which can be expressed as $X_i = \{x_j \mid x_j \in [0, 1], j \in [1, 64] \cap \mathbb{Z}\}$. The signal form in Fig. 1(b) loses information between adjacent cycles compared to the continuous signal in Fig. 2(a). However, it reduces the interference of non-pathological factors, such as heart rate and contact pressure, on the results of the analysis.

To better establish an analytical model that conforms to the TCM theory, we further simplified the data. Evidently, for different samples, the number of available single cycles is not the same because of the difference in sampling time and noise. In this study, we calculated the average cycle shown in Fig. 2(b) for each sample, which can be described as follows:

$$\overline{X} = \frac{\sum_{i=1}^{L} X_i}{L} \qquad (1)$$

where L represents the number of valid cycles per sample. Different samples may have different values owing to factors such as signal length and noise.

Compared with the signals in Figs. 1(b) and 2(a), the average cycle lost some information, but retained the key TCM information such as main waves, tidal waves, and replay waves. Furthermore, the average cycle also eliminated some noise in the signal to a certain extent and enhanced the key information. Therefore, it is reasonable to choose the average cycle as the pulse waveform for subsequent analyses.

## 3. Related works

3.1. Gaussian mixture model

The radial artery pulse waveform is a composite of the ascending and descending limbs created by systole and diastole. The amplitude, position, duration, and other information of each peak in the pulse waveform represent different physiological significance. The Gaussian function was used to fit the individual peaks in the pulse waveform owing to their similarity in shape. Previous studies have shown that the parameters of the Gaussian function are correlated with the physiological activity of the heart [5].

A basic *n*-term GMM can be expressed as follows:

$$f(x \mid A_1, \mu_1, \sigma_1 \cdots A_n, \mu_n, \sigma_n, \varepsilon) = \sum_{i=1}^{n} A_i e^{-\left(\frac{x-\mu_i}{\sigma_i}\right)^2} + \varepsilon \qquad (2)$$
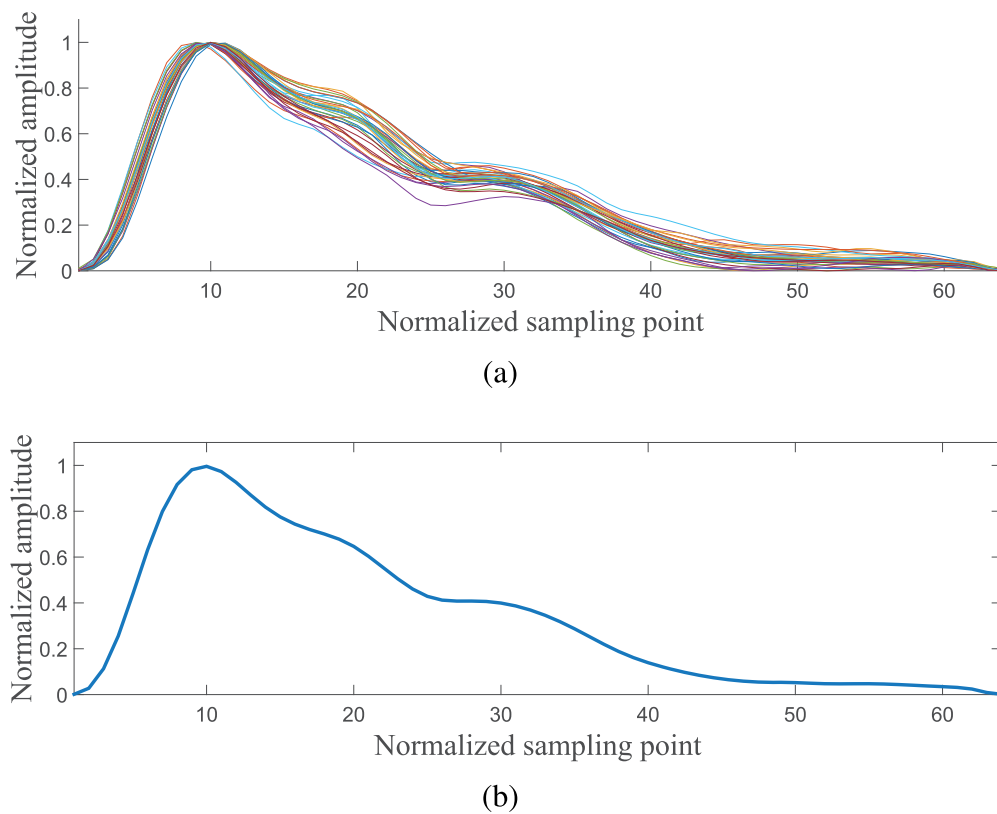
Fig. 2. Normalized single cycle pressure wrist pulse signal after segmentation: (a) all the segmented cycles and (b) average cycle of all the segmented cycles.
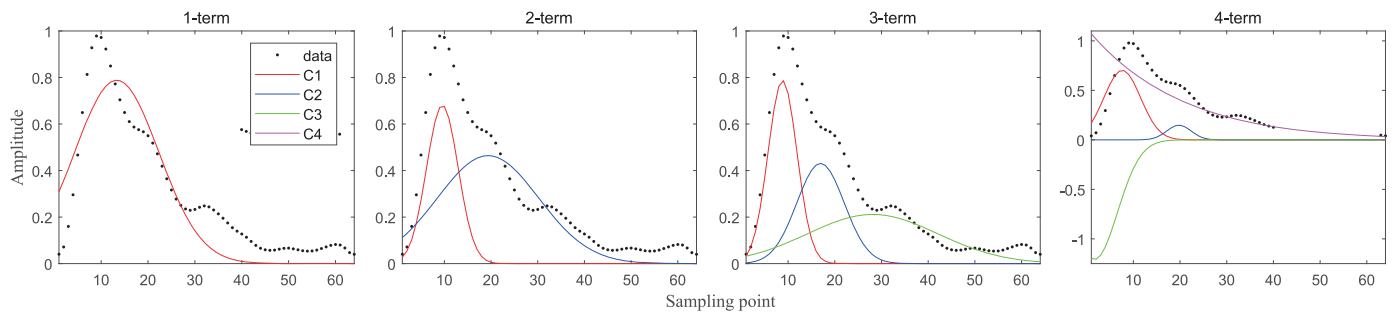
Fig. 3. Fitting components of the *n*-term GMM, *n*=1, 2, 3, 4. Each component is a Gaussian function, described by parameters A_i, μ_i and σ_i. The $\|\varepsilon\|$ values of these four models are 0.9787, 0.4788, 0.2233, and 0.1632, respectively. The label *data* in the legend represents raw data, and the labels $C1, C2, C3$ and $C4$ represent different components.

Each term of the Gaussian function in Eq. (2) represents a component associated with the peak in the waveform. The parameter A_i determines the amplitude of the *i*th component, μ_i represents the phase of the *i*th component relative to the starting point, σ_i represents the width of the *i*th component in the time dimension, and ε denotes the residue. Usually, these parameters can be obtained using the nonlinear least squares method.

Previous studies used different values of the number of Gaussian functions in Eq. (2). Because of the different working principles and collecting positions of the sensors, there are differences in the shape of the pulse waveform signals collected by different sensors. In the work in [5], a two-term GMM was adopted to model the radial artery Doppler ultrasound pulse signal, whereas in the study in [6], a three-term GMM was used to fit the radial artery pulse pressure waveform. Although some samples may not be clear on some peaks, the radial artery pulse pressure waveform signal used in this study is considered to contain three major peaks: the main wave, tidal wave, and dicrotic wave.

Fig. 3 shows the fitting results of the GMM with different numbers of items, and $\|\varepsilon\|$ is used to measure the fitting effect. The one-term model is a complete fitting of the waveform, not a description of the specific peak. $C1$ of the two-term model is a representation of the main peak, and $C2$ is a description of the remaining information comprising tidal and dicrotic waves. For the three-term model, $C1$ and $C2$ can have an approximate fitting for the shape and position of the main wave and tidal wave, respectively. Similar to $C2$ in the two-term model, $C3$ of the three-term model is also a description of the dicrotic wave and the remaining information. However, when the value of n reaches 4, as shown in Fig. 3, the four-term model over-represents the specific peaks. $C1$, $C3$ and $C4$ all tend to describe the main wave, which reduces the ability to describe other parts and introduces more errors to other parts. Although $\|\varepsilon\|$ decreases gradually as *n* increases, the components do not have a clear physiological significance when *n* exceeds 3.

The Gaussian function was selected as the model fitting the pulse waveform because its bell curve is similar to the shapes of

the peaks in the pulse waveform [5]. However, this symmetrical bell-shaped structure also limits further detailed representation of the pulse waveform. As a physiological signal, the peaks in the pulse waveform are not completely symmetrical. In addition, owing to the shape constraints, the Gaussian curve introduces additional components to other positions when representing a specific position. The adjustability of the Gaussian curve is insufficient because of the limited number of parameters.

3.2. Discrete Fourier series model

According to the Fourier analysis theory, the aperiodic signal can be expressed as a discrete time Fourier transform. For a real signal, the transform can be further transformed into a trigonometric series. Compared with signals such as electrocardiograph (ECG) and electroencephalograph, the pulse waveform is smoother and can be represented by the trigonometric Fourier series.

The DFSM of the pulse waveform can be described as:

$$
\begin{aligned}
f(x|\omega_0, a_0, a_1, b_1 \ldots, a_n, b_n, \varepsilon) \\
= \sum_{k=-n}^{+n} a_k e^{jk\omega_0 x} + \varepsilon \\
= a_0 + \sum_{k=1}^{n} a_k \cos k\omega_0 x + b_k \sin k\omega_0 x + \varepsilon
\end{aligned}
\tag{3}
$$

For the model shown in Eq. (3), parameter a_0 is the direct current and $\omega_0 = 2\pi/T$, where T is the length of the signal. With an increase in k, the frequency of the component gradually changes from low to high, and the physical meaning represented by the component changes from contour information to detailed information. By adjusting the values of a_k and b_k, the model changes the amplitude and shape of the sine and cosine to better represent the pulse waveform.

In contrast to the GMM, which focuses on fitting peaks with important physiological significance in the pulse waveform, the DFSM represents the components of different frequencies in the signal. Although it is not as intuitive as the GMM for physiological information, the DFSM is more robust to the shape, peaks, and noise of the pulse waveform.

Fig. 4 shows the fitting performance of the different models; the original data used in Fig. 4 are the same as those used in Fig. 3. As shown in Fig. 4(a), the fitting curve of the six-term DFSM used in [8] is basically coincident with the original data. The $\|\varepsilon\|$ of this model is 0.0747, which is smaller than that of commonly used GMMs.

Although the DFSM can achieve smaller fitting errors, the physiological significance of the fitted components shown in Fig. 4(b) is not as evident as that of the GMM. These two methods have their own advantages in terms of pulse waveform representation, but their limitations also limit further improvement of the performance. Thus, the combination of these two models to describe the pulse waveform using their respective advantages would be a significant option.

4. Sparse decomposition of the pulse waveform

4.1. Gabor function

Although we can clearly see the energy of each frequency contained in a signal from the Fourier transform used in [15] and [16], this transform cannot describe the characteristics of the specific position of the signal. The transmission times of different signals and the duration of transmission are difficult to determine. The lack of time-domain information makes Fourier analysis vulnerable and error-prone. In fact, the pulse waveform is composed of several different types of physiological activities, and it is useful
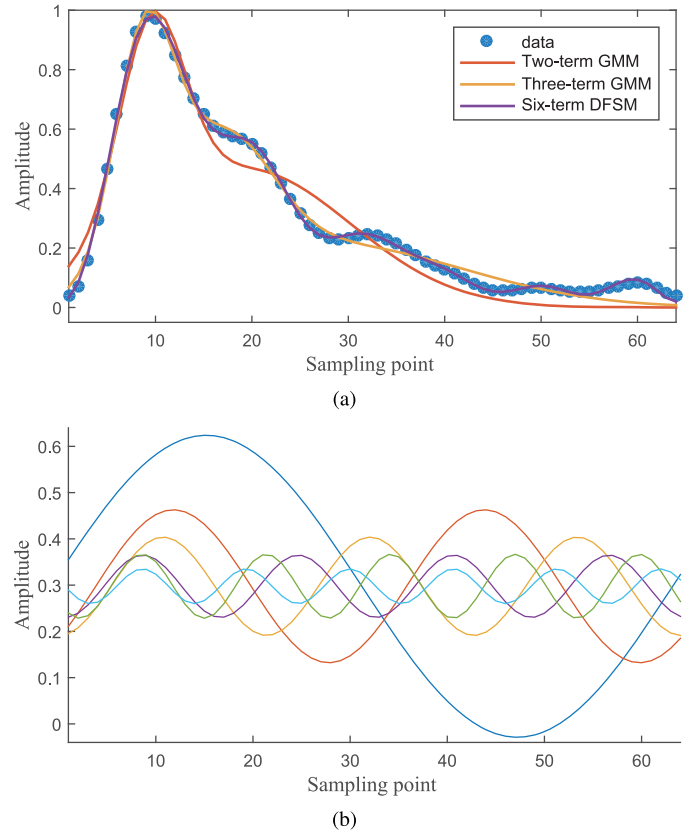
Fig. 4. Comparison of fitting performance between GMM and DFSM: (a) fitted curves of two-term GMM, three-term GMM, and six-term DFSM; (b) fitting components of the six-term DFSM.

to know the main frequency characteristics in specific time periods. For this time-frequency localization requirement, the Fourier transform is powerless.

To design a transform that provides the time-frequency representation of the signal, the windowed Fourier transform is proposed. The basic idea of the windowed Fourier transform is to divide the signal into many small time intervals and analyze each time interval using the Fourier transform. The processing method involves adding a sliding window $g(x - \mu)$ to the signal $f(x)$, such as $g(x - \mu)f(x)$, and then performing a Fourier transform. Therefore, the windowed Fourier transform can be expressed as:

$$
G(\mu, \omega) = \int_{-\infty}^{+\infty} f(x)g(x - \mu)e^{-j\omega x}dx
\tag{4}
$$

The time window function $g(x - \mu)$ implements windowing and panning near μ. Usually, the window function is a real dual function whose energy is concentrated at a low frequency. If the window function chooses the so-called bell-shaped function, which quickly approaches 0 in $t > t_0$, after the signal $f(x)$ is multiplied by the smoothly moving window function $g(x - \mu)$, the signal other than the neighborhood of $x = \mu$ is effectively suppressed. Therefore, the result of performing the Fourier transform on $f(x)g(x - \mu)$ reflects the spectrum information near the time $x = \mu$, thus achieving the purpose of time-domain localization.

The window function can utilize the Hanning window, Hamming window, Gaussian window, etc. When the window function of the windowed Fourier transform takes a Gaussian window function, it is called the Gabor transform. The basis function of the Gabor transform can be rewritten as:

$$
g_a(\delta, \mu, \omega) = \frac{1}{\delta\sqrt{2\pi}} e^{\frac{(x - \mu)^2}{2\delta^2}} e^{i\omega x}
\tag{5}
$$

The parameters δ, ω, and μ represent the modulation, expansion and displacement of the basis function, respectively.

The Gaussian function was chosen as the window function because its Fourier transform is still a Gaussian function. The Gaussian function can be simplified to $g(x) = e^{-ax^2}$, and its Fourier transform is:

$$
\begin{aligned}
F(\omega) &= \int_{-\infty}^{+\infty} g(x) e^{-j\omega x} dx = \int_{-\infty}^{+\infty} e^{-ax^2} e^{-j\omega x} dx \\
&= \int_{-\infty}^{+\infty} e^{-(ax^2 + j\omega x)} dx = e^{-\frac{\omega^2}{4a}} \int_{-\infty}^{+\infty} e^{-(\sqrt{a}x + \frac{j\omega}{2\sqrt{a}})} dx \\
&\xrightarrow{u = \sqrt{a}x + \frac{i\omega}{2\sqrt{a}}} e^{-\frac{\omega^2}{4a}} \int_{-\infty}^{+\infty} e^{-u^2} \frac{1}{\sqrt{a}} du \\
&= \frac{2}{\sqrt{a}} e^{-\frac{\omega^2}{4a}} \int_{0}^{+\infty} e^{-u^2} du = \sqrt{\frac{\pi}{a}} e^{-\frac{\omega^2}{4a}}
\end{aligned}
\tag{6}
$$

As observed, the transformed Gaussian function only changes the morphology. This makes the Fourier inverse transform also localized with a Gaussian window function, which also reflects the localization of the frequency domain.

Eq. (5) contains a wave with a complex number form, $e^{i\omega x}$, which is not conducive to the representation of the real signal. To better represent the pulse waveform in the time domain, the wave needs to be converted into other forms without complex numbers. According to Euler's formula, $e^{ix} = cos(x) + isin(x)$, the wave can be converted to a trigonometric form of a complex number, and Eq. (5) can be rewritten as:

$$
g_a(\delta, \mu, \omega) = \frac{1}{\delta\sqrt{2\pi}} e^{-\frac{(x-\mu)^2}{2\delta^2}} (cos(\omega x) + isin(\omega x))
\tag{7}
$$

Thus, Eq. (7) is the complex representation of the Gabor transformation basis function. We can split this equation into real and imaginary cores according to the real and imaginary parts:

$$
g_a(\delta, \mu, \omega)_{real} = \frac{1}{\delta\sqrt{2\pi}} e^{-\frac{(x-\mu)^2}{2\delta^2}} cos(\omega x)
\tag{8}
$$

$$
g_a(\delta, \mu, \omega)_{imag} = \frac{1}{\delta\sqrt{2\pi}} e^{-\frac{(x-\mu)^2}{2\delta^2}} sin(\omega x)
\tag{9}
$$

In our applications, only the real part of the basis function is necessary. The main difference between the real and imaginary parts is in the trigonometric function: one is modulated by cosine and the other is modulated by sinusoidal. The adjustment of the phase of the trigonometric function can compensate for this difference and result in more morphological changes. After adding a parameter υ that adjusts the phase of the cosine function, Eq. (8) can be modified as follows:

$$
g_a(\delta, \mu, \omega, \upsilon)_{real} = \frac{1}{\delta\sqrt{2\pi}} e^{-\frac{(x-\mu)^2}{2\delta^2}} cos(\omega x + \upsilon)
\tag{10}
$$

Eq. (10) has four tunable parameters and does not have a complex number. Because the equation is derived from the Gabor transform, it is usually referred to as the Gabor function. The set of

parameters can be represented as $\lambda = (\delta, \mu, \omega, \upsilon)$, and the parameters δ, μ, ω, and υ represent the scaling, translation, frequency, and phase of the corresponding signal, respectively.

Eq. (10) can be considered as a Gaussian function modulated by a trigonometric function. It contains the basic elements of both the GMM and the DFSM, which can complement each other in shape and compensate for the deficiencies of the two models. The cosine function can change the symmetric structure of the Gaussian function, thereby reducing the introduction of excess components, and also enhance the representation of the specific peaks by a Gaussian function and eliminate the influence on other positions through the Gaussian window. Therefore, in theory, the components produced by the Gabor function provide a better representation of the pulse waveform than those of GMM and DFSM.

Fig. 5 shows the four components generated by the Gabor function. These components are no longer limited to the upper and lower symmetry of the trigonometric function and the left and right symmetrical structures of the Gaussian function. Moreover, the range of representation of the trigonometric functions is well controlled. In general, compared with the model containing only Gaussian or trigonometric functions, the Gabor function can represent the specific peaks and also the contour information, and its shape is more changeable.

4.2. Sparse decomposition of the pulse waveform

Sparse decomposition is a commonly used signal analysis method that represents most or all of the original signals with a linear combination of fewer basic signals [17]. It first builds an over-complete dictionary and then uses as few atoms as possible in the dictionary to represent the original signal. The selected atoms are considered to make it easier to obtain the information contained in the original signal, which is more convenient for further processing of the signal, such as denoising, compression, and coding. Raj presented a feature extraction method using the sparse representation technique to efficiently represent the different ECG signals for the automated recognition of cardiac arrhythmias [18].

To represent the pulse waveform by the components generated by the Gabor function, we used the sparse approximation method. Given a set $D = \{g_k; k = 1, 2, \ldots, K\}$, whose elements are unit vectors that span the entire Hilbert space, $H = \mathbb{R}^N$. If $K \geq N$, then D is called an over-complete dictionary, and its elements are called atoms. For any signal $f \in H$, the sparse approximation selects m atoms in D to represent signal f:

$$
f_m = \sum_{\gamma \in I_m} c_\gamma g_\gamma
\tag{11}
$$

where I_m is the subscript set of g_γ, $m \ll N$ and $card(I_m) = m$. The approximation error can be defined as:

$$
\varepsilon_m(f, D) = \|f - f_m\|
\tag{12}
$$

From the perspective of the sparse approach, we expect that $\varepsilon_m(f, D)$ can be sufficiently small, and the value of m is also the
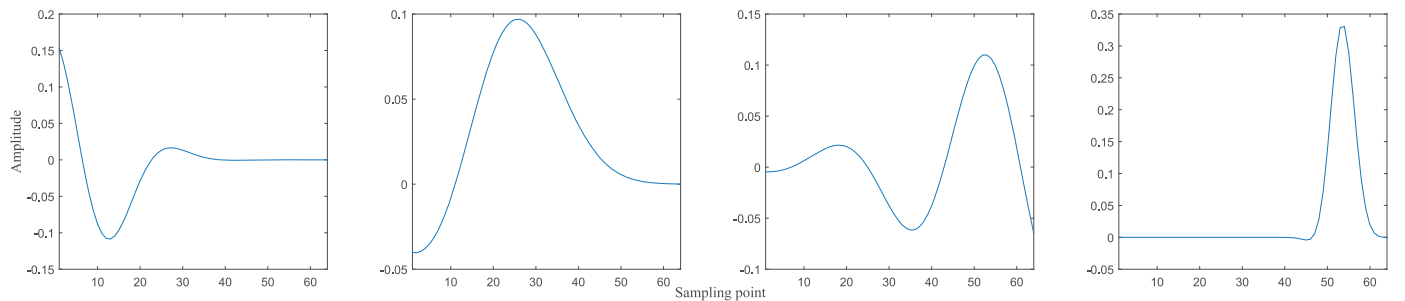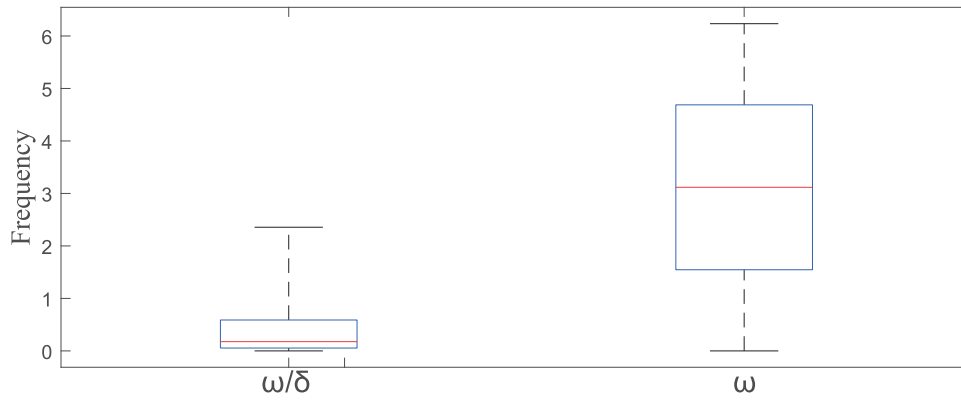

Fig. 5. Four components of different shapes generated by the Gabor function.

Fig. 6. Box plot depicting the atoms distribution of ω/δ and ω. On each box, the red central line indicates the median, and the bottom and top edges of the box indicate the 25th and 75th percentiles, respectively. Whiskers represent minimum and maximum values. (For interpretation of the references to colour in this figure legend, the reader is referred to the web version of this article.)

smallest. Therefore, finding the sparsest signal representation is equivalent to solving the following problem:

$$X \text{minimiz } \|c\|_0 \text{ subject to } f = \sum_{k=1}^{K} c_k g_k \qquad (13)$$

where $\|c\|_0$ is the number of non-zero terms in sequence c_k.

Therefore, this problem can be divided into two steps to represent the pulse waveform as a combination of a series of Gabor components. The first step is to build a suitable over-complete atom dictionary based on the characteristics of the pulse waveform using the Gabor function. Then, for each sample, a linear combination of the Gabor atoms is selected from the over-complete dictionary such as to minimize $\|c\|_0$.

To build an over-complete dictionary, it is necessary to determine the upper and lower bounds and the discretization method for the parameters of the Gabor function. In this study, we adopted a discrete strategy similar to that in [19] and optimized the method based on the characteristics of the pulse signal. Therefore, we first rewrite Eq. (10) into the following form:

$$g_a(\delta, \mu, \omega, \upsilon) = \frac{1}{\sqrt{\delta}} e^{-\pi \frac{(x-\mu)^2}{\delta^2}} cos(\omega x + \upsilon) \qquad (14)$$

Since the constant term $\frac{1}{\sqrt{2\pi}}$ is the same for each atom and can be reflected by subsequent sparse decomposition coefficients c_k, it can be omitted from Eq. (10). In [19], the parameters are discretized as $\lambda = (a^j, pa^j \Delta\mu, ka^{-j}\Delta\omega, i\Delta\upsilon)$, with $a = 2$, $\Delta\mu = 1/2$, $\Delta\omega = \pi$, $\Delta\upsilon = \pi/6$, $0 < j \leq log_2 N$, $0 \leq p < N2^{-j+1}$, $0 \leq k < 2^{j+1}$, $0 \leq i \leq 12$, where N is the length of the signal. Finally, we can get an atom dictionary with size $L_D = \sum_{j=1}^{log_2 N} \sum_{p=0}^{N2^{-j+1}-1} \sum_{k=0}^{2^{j+1}-1} \sum_{i=0}^{12} 1 = 19968$.

However, the atom dictionary generated according to this discrete criterion was specifically developed for voiced unvoiced speech discrimination in noise. The major difference between a speech signal and a pulse waveform signal is that the speech signal contains a large number of peaks, and the peaks change more dramatically. In our application, we expect the atom to have a unimodal structure to better decompose the smooth pulse waveform signal and better represent the specific peaks. Under the premise of maintaining the discretization method unchanged, it is necessary to reduce the value of ω to increase the cycle length of the cosine function, thereby reducing the number of peaks in the atom. Thus, we further rewrite Eq. (14) as:

$$g_a(\delta, \mu, \omega, \upsilon) = \frac{1}{\sqrt{\delta}} e^{-\pi \frac{(x-\mu)^2}{\delta^2}} cos\left(\frac{\omega}{\delta} x + \upsilon\right) \qquad (15)$$

Fig. 6 shows a box plot of the atom distribution with ω/δ and ω. Compared with ω in Eq. (14), ω/δ has a smaller upper bound,

which means that the number of peaks in the atom can be effectively reduced. More importantly, the discrete intervals of ω/δ become smaller at low frequencies, allowing more low-frequency atoms to be obtained in different shapes. Therefore, under the condition that the discrete method is constant, the atoms generated according to Eq. (15) are more in line with our requirements.

After producing an over-complete atom dictionary, it is necessary to select the optimal atom combination in the atom dictionary, which can guarantee the minimization of $\|c\|_0$. In this study, we used orthogonal matching pursuit (OMP) to select the atoms that represent the pulse waveform signal [20]. The basic idea of the OMP algorithm is to select an atom most matched with the signal f from the over-complete atom dictionary to construct a sparse approximation $c_{\gamma_0} g_{\gamma_0}$, and calculate the signal residual R^0. Then, it continues to select the atom that best matches the R^0 and iterates repeatedly until a certain termination condition is reached. The signal f can be represented by the linear combination of the selected atoms and the final residual as follows:

$$f = \sum_{k=0}^{M-1} c_{\gamma_k} g_{\gamma_k} + R^M \qquad (16)$$

Therefore, after neglecting the residual term R^M, the signal can be represented in the form of a vector as $\mathbb{F}_M = (c_{\gamma_0} g_{\gamma_0}, \ldots, c_{\gamma_{M-1}} g_{\gamma_{M-1}})$. In this study, we used this vector for automated computer-aided analysis of the pulse waveform; the value of M was determined, as described in the next section, and the best combination of components was selected to improve the classification performance.

5. Results

5.1. Dataset and measurement

As shown in Table 1, the dataset of pulse wave signals used was collected from Guangdong Provincial Hospital of Traditional Chinese Medicine, including five classes, totaling 2074 samples. The dataset consists of 828 health samples (HE), 267 diabetes samples (D), 462 cardiac disease samples (C), 233 hypertension samples (HY), and 284 nephropathy samples (N). The health samples, which did not suffer from any disease, were collected from the medical examination center of the hospital, and the disease samples were collected from the ward of the hospital. Nephropathy mainly includes chronic kidney disease and nephrotic syndrome, diabetes mainly includes type II diabetes, and cardiac disease mainly includes coronary heart disease, arrhythmia, and bradycardia. Some samples may have multiple disease labels. We asked the doctor

Table 1
Dataset of pulse wave signals.

		HE	D	C	HY	N
Age	1~20	27	1	8	1	10
	21~40	680	20	220	11	45
	41~60	33	101	122	89	112
	>60	4	140	106	123	113
	Unrecorded	84	5	6	9	4
Gender	Male	396	109	301	91	153
	Female	347	153	155	133	127
	Unrecorded	85	5	6	9	4
Total		828	267	462	233	284

to distinguish the main diseases and complications of the sample, and used the main diseases as labels in this study. Each sample was first preprocessed according to the method described in Section II, and then sparse decomposition was performed according to the method in Section IV.

Table 2 shows the division of the training and test sets for the different tests. For each disease group, 80% of the samples were selected as training sets and 20% as test sets for binary classification. To maintain the balance of samples that can better train and test the model, the same number of healthy samples was selected. Columns 2 and 3 in Table 2 show the division of the training and test sets for multi-classification based on balanced and imbalanced samples, respectively. Because the number of hypertension samples was the lowest, 80% of hypertension samples were selected as the training set, 20% of hypertension samples as the test set, and the same number of samples was adopted for the other classes in the balanced samples case. In the imbalanced samples case, 80% of the samples were selected for the training set and 20% for the test set, which leads to an imbalance between classes. Moreover, to reduce accidental errors caused by sample selection and division of the training and test sets, all the tests in this study were repeated 20 times. For each time, the training and test sets were randomly redivided.

To measure the results objectively, the average accuracy was adopted to measure the performance of binary classification, and the average F1 score was adopted to measure the performance of multi-classification, which was calculated as follows:

$$accuracy = \frac{\overline{TP} + \overline{TN}}{\overline{TP} + \overline{TN} + \overline{FP} + \overline{FN}} * 100\%$$

$$F1\ score = \frac{1}{5} \sum_{c=1}^{5} \frac{2 * \overline{P_c} * \overline{R_c}}{\overline{P_c} + \overline{R_c}}, \text{ where}$$

$$\overline{P_c} = \frac{\overline{TP_c}}{\overline{TP_c} + \overline{FP_c}}$$

$$\overline{R_c} = \frac{\overline{TP_c}}{\overline{TP_c} + \overline{FN_c}}$$

$\overline{TP}$, $\overline{TN}$, $\overline{FP}$ and $\overline{FN}$ represent the average number of true positives, true negatives, false positives, and false negatives in the prediction result, respectively. $\overline{P_c}$ and $\overline{R_c}$ are the precision and recall of class c.

5.2. Feature optimization

We used three criteria to select and optimize the features gradually. The first criterion is the residual R^M. When the representation residual gradually converges and approaches 0, the selected representation component already contains most of the information of the original signal. At this time, the decomposition process can stop and the selected component can be used as the candidate feature. The second criterion is the separability of the selected components. We expected to choose highly separable decomposing components as features to better distinguish people with different health states. The third criterion is the classification performance. After analyzing the representation residual and separability of the components using the first two criteria, the final feature vector can be determined in combination with the classification performance.

Fig. 7 shows the tendency of the average residual $\overline{R^M}$ with M of the samples. The residual $\overline{R^M}$ quickly converges before $M = 6$, and then the convergence speed gradually decelerates. In addition, because the average residuals of two-term GMM, three-term GMM, and six-term DFSM are 0.0413, 0.0254, 0.0132, respectively, it is reasonable to choose the component with $M \leq 10$ for detailed analysis. Thus, we chose $\overline{R^5} = 0.0135$, which reached the same performance as the six-term DFSM in terms of fitting the pulse waveform.

Because the extracted sparse decomposition features are used for classification, we used a sample-based separability criterion to further screen the features. The criterion can be described as Eq. (17), where S_m is the global covariance matrix, S_w is the intraclass scatter matrix, and the symbol tr indicates the trace of the matrix. The larger the value of J, the more the samples of each class are clustered around the mean in the feature space, and the different classes are separated from each other.

$$J = \frac{tr(S_m)}{tr(S_w)} \tag{17}$$

We calculated the separability of each item in Eq. (17) for HE/D(J1), HE/C(J2), HE/HY(J3), and HE/N(J4). Fig. 8(a) shows the separability tendencies of the selected Gabor components. For J1, J3 and J4, the separability reached its maximum at the second atoms and then gradually decreased. For J2, the separability reached its maximum at the first atom and then decreased. For these four binary classifications, when $M > 10$, the separability of the selected components approached 1, that is, they were essentially non-separable. Then, we used all samples to calculate the separability, and the results are shown in Fig. 8(b). Component 2 obtained the best class separability, followed by components 1, 4, 3, 6, and 5. After component 8, the value of J remained basically unchanged, and the complete component separability was sorted from high to low as 2, 1, 4, 3, 6, 5, 8, 7, 9, 15, 21, 13, 14, 10, 16, 17, 28, 27, 22, 18, 24, 19, 12, 23, 29, 25, 20, 11, 30, 26. Thus, the first nine components with the better separability were the decomposition results when $M = 9$. Therefore, it is reasonable to select the first 15 components for further study, regardless of the degree of reduction of the original signal or the separability of the selected components.
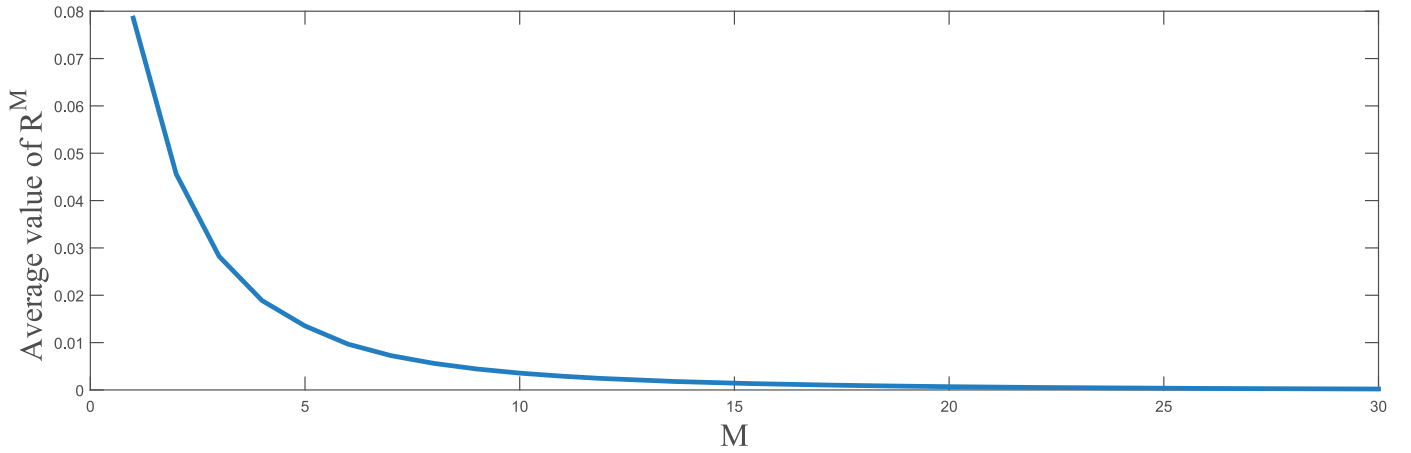
Table 2
Division of training and test sets.

binary		multi-class 1		multi-class 2	
class	training/test	class	training/test	class	training/test
(HE,D)	(214,214)/(53,53)	(HE, D, C,HY,N)	(187,187,187,187,187)/ (46,46,46,46,46)	(HE,D,C,HY, N)	(663,214,370,187,228)/ (165,53,92,46,56)
(HE,C)	(370,370)/(92,92)				
(HE,HY)	(187,187)/(46,46)				
(HE, N)	(228,228)/(56,56)				

Fig. 7. First criterion for component selection: tendency of the average residual R^M with M.

To continue to optimize the combination of selected components, we performed four binary classification tests for HE/D, HE/C, HE/HY, and HE/N using feature vectors of different lengths. The feature vectors were composed of multiple components, and the components were sequentially added to the feature vector in the order of selection, such as $\mathbb{F}_0 = (c_{\gamma_0} g_{\gamma_0})$ and $\mathbb{F}_1 = (c_{\gamma_0} g_{\gamma_0}, c_{\gamma_1} g_{\gamma_1})$. In all four tests, the support vector machine-radial basis function (SVM-RBF) classifier was used, which can solve the problem of data classification of high-dimensional small samples [21]. To optimize the classification model of the SVM-RBF classifier, we used the grid search method to determine the optimal parameters. Fig. 9 shows the classification results for the different feature vectors. The classification accuracy of feature vectors composed of multiple components tended to be stable as the number of added components increased.

Evidently, for different binary classifications, the combinations of components that can obtain the best accuracy are not the same. However, because the separability was mainly reflected in the first few selected components, we constructed a suboptimal general feature vector containing the first few components. In this study, the first nine selected components were used to form the suboptimal general feature vector for subsequent analysis.

The pulse waveform and its decomposition components are shown in Fig. 10. We can qualitatively analyze the physiological significance of each component. The first component can be considered as a description of the overall contour information of the signal. The second component describes the main wave and tidal wave, and reflects their relative positions. The third component is the representation of the dicrotic wave, and the fourth component represents the tail of the signal. The fifth and sixth components can be regarded as complementary representations of the main wave and dicrotic wave, and the remaining three components are complementary descriptions of the signal. Thus, the main physiological information contained in the pulse waveform can be reflected in the first nine components.

5.3. Binary classification with SVM-RBF

In this section, SVM-RBF is used to compare the binary classification performance of seven types of features, including DFSM, PCA, Hilbert, two-term GMM, three-term GMM, wavelet energy, and the proposed method. The SVM-RBF is one of the most commonly used classifiers in previous studies of pulse signal classification and can train a better decision surface with a small number of samples. Table 3 shows the classification performance of the different features using the SVM-RBF.

For SVM-RBF, the test settings were the same as those in Section 5.2, and the parameters for each type of feature were optimized. As observed, the accuracy of the proposed method was 1.32%, 2.55%, 2.6% and 2.01% higher than that of the other features on SVM-RBF for HE/D, HE/C, and HE/HY, respectively.

The ability of the proposed method to distinguish disease pulse signals from healthy pulse signals was verified by binary classification. The proposed method achieved the highest accuracy for most classifications. Therefore, the proposed pulse signal representation technique can be considered more efficient for representing the pathological information in the pulse signals.

5.4. Multi-classification of the pulse signals

The multi-classification performances of the different types of features are compared in this section. The first test used balanced training and test samples, which were divided as shown in the second column in Table 2. The second test used imbalanced training and test samples, which were divided as shown in the third column of Table 2. To eliminate the dependence of the proposed method on the classifier and verify the generality of the proposed method, four classifiers were selected to evaluate the multi-classification performance of the different features: random forest (RF) [22], K-nearest neighbor (KNN), discriminant analysis classifier (DAC) [23], and SVM-RBF. In addition, considering the effectiveness of deep learning technology and the timing characteristics of pulse wave signals, the architecture of Keras + Tensorflow was also adopted, using a recurrent neural network (RNN) and long short-term memory (LSTM) as classifiers [24]. The main parameters were optimized by grid, in which the range of network layers was (1,2), and the range of nodes was (64,128,256).

Table 4 shows the multi-classification performance of the different features measured by the F1 score for the balanced samples. As one of the most effective classification features in previous studies, the PCA feature obtained the best classification accuracy for RF, DAC, SVM, RNN, and LSTM classifiers. However, the accuracies of Gabor decomposition features on the six classifiers reached 44.89%, 41.26%, 43.89%, 46.52%, 46.09%, which were 3.93%, 4.39%, 4.17%, 3.87%, 3.92% and 4.35% higher than those of PCA, respectively. In summary, for balanced samples, the best combination of features and classifiers was Gabor+SVM-RBF.

The multi-classification performance measured using the F1 score for the imbalanced samples is shown in Table 5. Although the imbalance of the training and test sets may cause significant interference to the learning process of the classifiers and lead to the non-objectiveness of the evaluation criteria, the results still re-
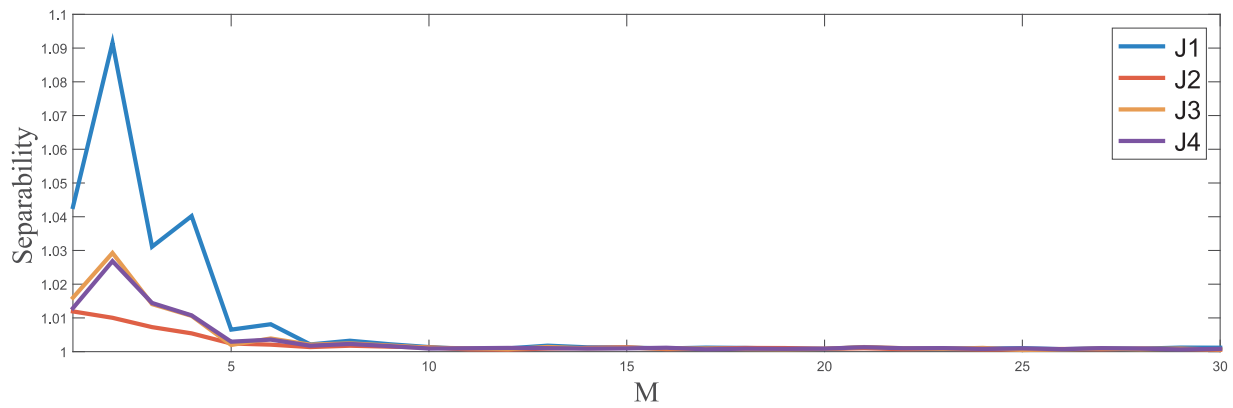
(a)
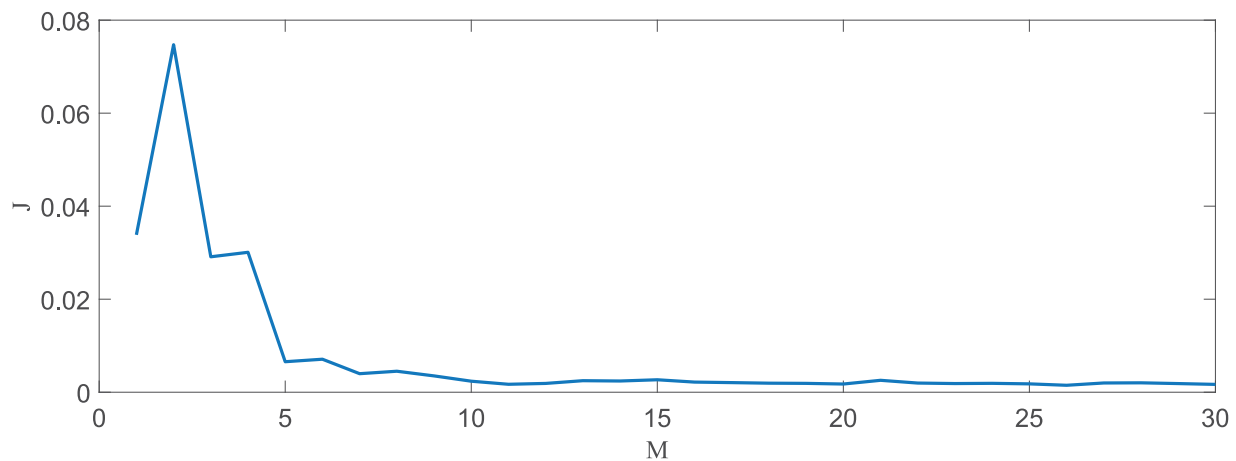
(b)

Fig. 8. Second criterion for component selection: (a) separability tendencies of the selected components for HE/D, HE/C, HE/HY, and HE/N. The legends J1, J2, J3, and J4 are the tendencies of HE/D, HE/C, HE/HY, and HE/N, respectively; (b) separability tendencies of the selected components for all samples.

Table 3
Average binary classification accuracy and standard deviation of different features with SVM-RBF.

|	HE/D	HE/C	HE/HY	HE/N
DFSM	90.61% (2.11%)	63.45% (±1.93%)	66.96% (±4.09%)	80.27% (±2.49%)
PCA	92.22% (±2.05%)	70.87% (±2.92%)	85.82% (±3.81%)	79.29% (±3.05%)
Hilbert	63.58% (±3.07%)	61.79% (±2.73%)	64.95% (±3.13%)	67.01% (±3.85%)
two-term GMM	86.56% (±3.24)	65.68% (±3.06%)	74.24% (±4.08%)	77.99% (±3.42%)
three-term GMM	63.96% (±2.54)	53.97% (±1.42%)	58.48% (±3.76%)	60.80% (±4.87%)
Wavelet energy	63.40% (±2.70%)	57.66% (±2.78%)	61.09% (±4.75%)	64.29% (±3.90%)
The Proposed	**93.54% (±1.77%)**	**73.42% (±2.96%)**	**88.42% (±3.95)**	**82.28% (±2.17%)**

Table 4
Average multi-classification accuracy and standard deviation of different features with balanced samples.

	RF	KNN	DAC	SVM	RNN	LSTM
DFSM	27.07%(±2.12%)	27.61%(±2.19%)	25.13%(±2.51%)	30.85%(±1.83%)	28.70%(±2.75%)	28.26%(±2.69%)
PCA	40.96%(±2.36%)	36.85%(±2.22%)	39.72%(±3.21%)	42.74%(±2.91%)	42.17%(±4.32%)	37.39%(±4.03%)
Hilbert	27.67%(±3.04%)	26.15%(±1.92%)	25.78%(±2.24%)	30.07%(±2.00%)	23.04%(±2.10%)	24.35%(±1.58%)
two-term GMM	36.59%(±2.57%)	35.74%(±2.89%)	22.24%(±2.67%)	35.80%(±2.63%)	26.96%(±1.60%)	23.48%(±0.64%)
three-term GMM	31.70%(±2.08%)	31.37%(±1.66%)	24.50%(±1.62%)	26.57%(±1.51%)	26.52%(±1.49%)	28.26%(±2.04%)
Wavelet energy	24.61%(±2.24%)	25.39%(±2.16%)	21.13%(±2.16%)	28.02%(±2.19%)	18.70%(±0.95%)	19.57%(±2.23%)
The Proposed	**44.89%(±2.69%)**	**41.26%(±3.05%)**	**43.89%(±2.29%)**	**46.52%(±2.06%)**	**46.09%(±1.72%)**	**41.74%(±3.55%)**

Table 5

Average multi-classification F1 score and standard deviation of different features with imbalanced samples.

	RF	KNN	DAC	SVM	RNN	LSTM
DFSM	0.2374(±0.0142)	0.2449(±0.0167)	0.1315(±0.0071)	0.1975(±0.0186)	0.1184(±0.0018)	0.1244(±0.0021)
PCA	0.3585(±0.0192)	0.3387(±0.0197)	**0.4048**(±**0.0276**)	0.4089(±0.0199)	0.3454(±0.0312)	0.3561(±0.0180)
Hilbert	0.2348(±0.0144)	0.2385(±0.0170)	0.1597(±0.0118)	0.2303(±0.0151)	0.1461(±0.0030)	0.1459(±0.0045)
two-term GMM	0.3516(±0.0192)	0.3403(±0.0153)	0.1187(±0.0087)	0.2202(±0.0118)	0.1180(±0.0052)	0.1144(±0.0004)
three-term GMM	0.3010(±0.0163)	0.2864(±0.0154)	0.1707(±0.0165)	0.2139(±0.0162)	0.1464(±0.0173)	0.1548(±0.0131)
Wavelet energy	0.2102(±0.0166)	0.2262(±0.0118)	0.1186(±0.0050)	0.1616(±0.0135)	0.1154(±0.0029)	0.1148(±0.0003)
The Proposed	**0.3865**(±**0.0142**)	**0.3859**(±**0.0189**)	0.4010(±0.0242)	**0.4242**(±**0.0186**)	**0.3526**(±**0.0203**)	**0.3800**(±**0.0289**)
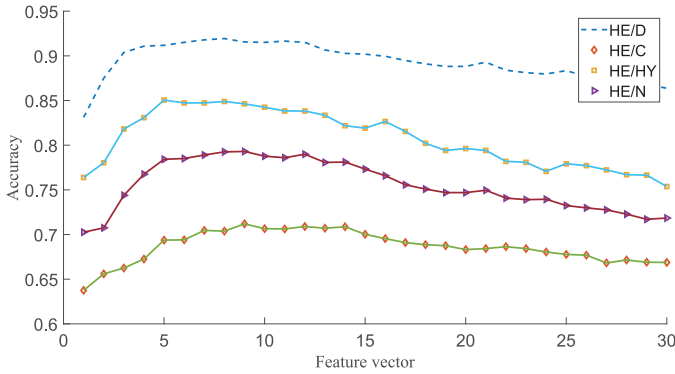
Fig. 9. Accuracy of binary classification using different feature vectors.

flect the classification performance of each feature to some extent. For the previous methods, the best performance on RF, DAC, SVM-RBF, RNN, and LSTM classifiers was achieved by the PCA feature, with F1 scores of 0.3585, 0.4048, 0.4089, 0.3454, and 0.3561, respectively; for the KNN classifier, two-term GMM feature achieved the highest classification performance, with an F1 score of 0.3403. Gabor decomposition features had values 0.0280, 0.0456, 0.0153, 0.0072, and 0.0239 higher than the best performance of previous methods on RF, KNN, SVM, RNN, and LSTM classifiers, respectively, but 0.0038 lower than the PCA feature on DAC classifiers. However,

Gabor features can be used in the SVM-RBF classifier, obtaining the highest F1 score of 0.4242.

Through the multi-classification of different features, we can draw the following conclusion: Gabor decomposition features can obtain the best classification results on most classifiers, whether based on balanced or unbalanced data. Although the F1 score of the Gabor decomposition feature is slightly lower than that of the DAC classifier with unbalanced data, overall, the Gabor decomposition features still achieved the best classification performance on the SVM-RBF classifier. Therefore, compared with the previously proposed methods, the sparse decomposition method of pulse waves based on the Gabor time-frequency atomic dictionary is advanced in the application of disease classification. In addition, on the RNN and LSTM classifiers, Gabor decomposition features also have certain advantages in classification performance, which can provide a better foundation for further combination with deep learning methods.

5.5. Time consumption

Since the Gabor dictionary is generated previously, the time consumption of the proposed method mainly depends on the time complexity of OMP which can be approximately represented as $O(kmn)$, where k is the number of the selected atoms, m and n are the size of the Gabor dictionary. As mentioned above, when $k = 9$, $m = 64$ and $n = 19968$, the average time consumption to extract the feature from an average cycle is 0.0075 seconds by the proposed method using MATLAB software package installed on Win-
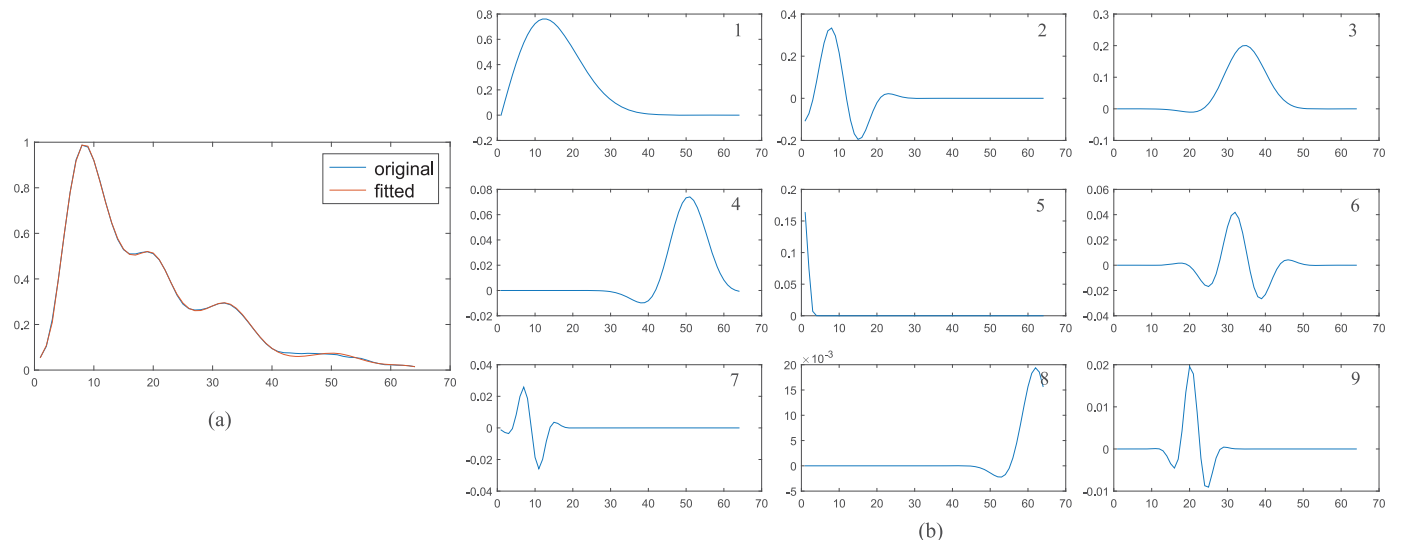
Fig. 10. Pulse waveform signal and its decomposition components. (a) Original pulse waveform signal and fitted signal using the first nine selected components. (b) Nine decomposition components ($c_{\gamma_k} g_{\gamma_k}$).

dows 10 platform, Intel Core TM i7-processor CPU 3.40 GHz and 64 GB of RAM.

5.6. Limitation

The samples in different groups are not balanced in age and gender. This unbalanced sample distribution may have a certain impact on the classification results. However, the comparison under the same conditions on the same database still has certain scientific significance and fairness. In the future, it is necessary to collect a database with more reasonable age and gender distribution.

Although the performance improvement of our proposed method in binary classification is not significant considering the standard deviation, it has advantages in physiological interpretability, and there is still room for improvement, such as building a more discriminative atomic library. On the other hand, our method also provides a competitive alternative feature for classification methods based on multi-feature fusion.

6. Conclusion

In this study, we proposed a novel representation method for the pulse waveform based on sparse decomposition using an overcomplete dictionary produced by the Gabor function. It decomposes the pulse waveform signal into several independent components with certain physiological significance, which can be considered as the representations of the main peak, tidal wave, dicrotic wave, and other meaningful information. The over-complete time-frequency dictionary used in this method is generated by the Gabor function, which combines the advantages of the GMM and DFSM. Compared with traditional representation methods, the proposed method can better describe the pulse waveform in shape and obtain a smaller representation error. The feature vector composed of the selected components is highly efficient and can be used for computerized pulse signal analysis and disease diagnosis. The method proves the scientific nature of using pulse waveforms to analyze the health state in TCM.

The results show that the different components have different classification performances for distinguishing between healthy people and people with diseases. Compared with previous pulse signal analysis methods, the method proposed in this study can also achieve better performance in disease diagnosis. In the binary classification of healthy and diseased pulse signals, the proposed method can achieve the best results for health/diabetes, health/cardiac disease, health/hypertension, and health/nephropathy with accuracies of 93.54%, 73.42%, 88.42% and 82.28%, respectively, which represent improvements of 1.32%, 2.55%, 2.6% and 2.01%, respectively, compared with the second-best method. The multi-classification performance of the different types of features was evaluated by six classifiers, and the proposed method obtained the highest classification performance with SVM-RBF for both balanced and imbalanced samples. In the case of balanced samples, the proposed method achieved the highest classification performance on all six classifiers, and the accuracy of the SVM classifier reached 46.52%. For unbalanced samples, the highest F1 score on the DAC classifier (0.4048) was obtained by PCA, but in the other five classifiers, the best performance was achieved by the proposed method, and the highest F1 score was 0.4242. In general, compared with single-cycle signal extraction methods such as DFSM [8], two-term GMM [5], and three-term GMM [6], our method resulted in less representation error and clear advantages in distinguishing people with different health states. Moreover, the classification performance of this method was also better than that of the PCA feature [9], which is extracted based on a single-cycle set, and Hilbert [10] and wavelet energy [11] features extracted from continuous pulse wave signals.

Future research can further optimize the structure of the Gabor function to build a dictionary that is more consistent with the characteristics of the pulse signal. On the basis of more accurate decomposition of pulse wave waveform, it is meaningful to explore the actual differences in waveform of different diseases. Moreover, for practical application environments, it is also beneficial to develop a feature fusion technology to improve multi-classification performance by using state-of-the-art features.

Declaration of Competing Interest

The authors claim that no conflict of interest exits in the submission of this manuscript, and the manuscript is approved by all authors for publication. This paper is further improved from one of our conference papers, the method is further optimized, and new experiments are added. The authors also claim that the paper has not been published or is under consideration for publication elsewhere.

Acknowledgments

References

[1] Sima, Qian, Pulse Diagnosis in Early Chinese Medicine, Cambridge University Press, 2010.

[2] J. Ostrowski, The secret of chinese pulse diagnosis, Orient. Med. J. 123 (1) (1996) 94–99.

[3] S. Lukman, Y. He, S.C. Hui, Computational methods for traditional chinese medicine: a survey, Comput. Methods Programs Biomed. 88 (3) (2007) 283–294.

[4] L. Xu, M.Q.-H. Meng, K. Wang, W. Lu, N. Li, Pulse images recognition using fuzzy neural network, Expert Syst. Appl. 36 (2) (2009) 3805–3811.

[5] Y. Chen, L. Zhang, D. Zhang, D. Zhang, Wrist pulse signal diagnosis using modified gaussian models and fuzzy c-means classification, Med. Eng. Phys. 31 (10) (2009) 1283–1289.

[6] C. Liu, D. Zheng, A. Murray, C. Liu, Modeling carotid and radial artery pulse pressure waveforms by curve fitting with gaussian functions, Biomed. Signal Process. Control 8 (5) (2013) 449–454.

[7] K.Y. Shin, T.B. Lee, S.O. Jin, S.H. Choi, S.K. Yoo, Y. Huh, J.U. Kim, J.Y. Kim, Characteristics of the pulse wave in patients with chronic gastritis and the healthy in korean medicine, in: Engineering in Medicine and Biology Society, 2012, pp. 992–995.

[8] Z. Jiang, D. Zhang, G. Lu, Radial artery pulse waveform analysis based on curve fitting using discrete fourier series, Comput. Methods Programs Biomed. (2018).

[9] W. Dimin, D. Zhang, L. Guangming, Generalized feature extraction for wrist pulse analysis: from 1-d time series to 2-d matrix, IEEE J. Biomed. Health Inform. 21 (4) (2017) 978–985.

[10] D. Zhang, K. Wang, X. Wu, B. Huang, Hilbert-Huang transform based doppler blood flow signals analysis, in: International Conference on Biomedical Engineering and Informatics, Bmei 2009, October 17–19, 2009, Tianjin, China, 2009, pp. 1–5.

[11] D. Zhang, L. Zhang, D. Zhang, Y. Zheng, Wavelet based analysis of doppler ultrasonic wrist-pulse signals, in: International Conference on Biomedical Engineering and Informatics, 2008, pp. 539–543.

[12] D. Wang, D. Zhang, G. Lu, A novel multi-channel wrist pulse system with different sensor arrays, IEEE Trans. Instrum. Meas. 64 (7) (2015) 2020–2034.

[13] D. Wang, D. Zhang, G. Lu, A robust signal preprocessing framework for wrist pulse analysis, Biomed. Signal Process. Control 23 (2016) 62–75.

[14] Z. Zhang, Y. Zhang, L. Yao, H. Song, A. Kos, A sensor-based wrist pulse signal processing and lung cancer recognition, J. Biomed. Inform. 79 (2018) 107–116.

[15] C.M. Huang, H.C. Chang, K. Shung-Te, T.C. Li, C.C. Wei, C. Chen, Y.T. Liao, F.J. Chen, Radial pressure pulse and heart rate variability in heat- and cold-stressed humans, Evid.-Based Complement. Alternat.Med. 2011, (2010-10-11) 2011 (1741–427X) (2010) 751317.

[16] L.Y. Wei, P. Chow, Frequency distribution of human pulse spectra, IEEE Trans. Biomed. Eng. BME-32 (3) (2007) 245–246.

[17] M. S, Z. Zhang, Matching pursuit with time-frequency dictionaries, IEEE Trans. Signal Process. 41 (1993) 3397–3415.

[18] S. Raj, K.C. Ray, Sparse representation of ecg signals for automated recognition of cardiac arrhythmias, Expert Syst. Appl. 105 (2018) 49–64.

[19] A.P. Lobo, P.C. Loizou, Voiced/unvoiced speech discrimination in noise using Gabor atomic decomposition, in: Acoustics, Speech, and Signal Processing, International Conference on, IEEE, 2003.

[20] Y.C. Pati, R. Rezaiifar, P.S. Krishnaprasad, Orthogonal matching pursuit: Recursive function approximation with applications to wavelet decomposition, in: Proceedings of 27th Asilomar conference on signals, systems and computers, IEEE, 1993, pp. 40–44.

[21] C.-C. Chang, C.J. Lin, LIBSVM: a library for support vector machines, ACM Trans. Intell. Syst.Technol. (TIST) 2 (3) (2011) 27.

[22] A. Liaw, M. Wiener, et al., Classification and regression by randomforest, R News 2 (3) (2002) 18–22.

[23] A. Alkan, M. Günay, Identification of EMG signals using discriminant analysis and SVM classifier, Expert Syst. Appl. 39 (1) (2012) 44–47.

[24] N. Ketkar, Introduction to Keras, Apress, 2017.